Controlled detection in composite nanoresonant array for surface plasmon resonance sensing

Lin Pang[1,*], Haiping M. Chen[1], Lilin Wang[2], Joseph M. Beechem[2], and Yeshaiahu Fainman[1]

[1] *Department of Electrical of Computer Engineering, University of California, San Diego, 9500 Gilman Drive, La Jolla, CA 92093, USA*

[2] *Genetic Systems, Life Technologies, 5781 Van Allen Way, Carlsbad CA 92008*

**lpang@ece.ucsd.edu*

Abstract: A composite nanoresonant structure is developed for sensitivity enhancement in biorecognition reactions by coupling between the localized resonance and the propagating surface plasmon polariton waves. The resonant structure was accomplished by combining holographic lithography with an oblique metallic deposition for cost-effective, large-area, and reconfigurable fabrication. The metallodielectric nanostructure was assembled with microfluidic channels and examined for biorecognition reactions, which showed pronounced improvement in the limit of detection compared to conventional nanohole array sensing configurations. The temperature influence on the binding affinity and the effectiveness of the control channel were also investigated to demonstrate the capability of the proposed composite nanoresonant surface plasmon resonance array sensor.

OCIS codes: (240.6680) Surface Plasmons; (130.6010) Sensors; (050.1950) Diffraction Gratings; (260.3910) Optics of Metals.

References and links

1. T. W. Ebbesen, H. J. Lezec, H. F. Ghaemi, T. Thio, and P. A. Wolff, "Extraordinary optical transmission through sub-wavelength hole arrays," Nature **391**(6668), 667–669 (1998).
2. C. Nylander, B. Liedberg, and T. Lind, "Gas detection by means of surface plasmon resonance," Sens. Actuators **3**(1), 79–88 (1982/83).
3. E. Stenberg, B. Persson, H. Roos, and C. Urbaniczky, "Quantitative determination of surface concentration of protein with surface plasmon resonance using radiolabeled proteins," J. Colloid Interface Sci. **143**(2), 513–526 (1991).
4. C. R. Lawrence, N. J. Geddes, D. N. Furlong, and J. R. Sambles, "Surface plasmon resonance studies of immunoreactions utilizing disposable diffraction gratings," Biosens. Bioelectron. **11**(4), 389–400 (1996).
5. A. G. Brolo, R. Gordon, B. Leathem, and K. L. Kavanagh, "Surface plasmon sensor based on the enhanced light transmission through arrays of nanoholes in gold films," Langmuir **20**(12), 4813–4815 (2004).
6. K. A. Tetz, L. Pang, and Y. Fainman, "High-resolution surface plasmon resonance sensor based on linewidth-optimized nanohole array transmittance," Opt. Lett. **31**(10), 1528–1530 (2006).
7. J. Homola, S. S. Yee, and G. Gauglitz, "Surface plasmon resonance sensors: review," Sens. Actuators B Chem. **54**(1–2), 3–15 (1999).
8. L. Pang, G. M. Hwang, B. Slutsky, and Y. Fainman, "Spectral sensitivity of two-dimensional nanohole array surface plasmon polariton resonance sensor," Appl. Phys. Lett. **91**(12), 123112 (2007).
9. P. Hanarp, M. Käll, and D. S. Sutherland, "Optical Properties of Short-Range Ordered Arrays of Nanometer Gold Disks Prepared by Colloidal Lithography," J. Phys. Chem. B **107**(24), 5768–5772 (2003).
10. T. Rindzevicius, Y. Alaverdyan, A. Dahlin, F. Höök, D. S. Sutherland, and M. Käll, "Plasmonic sensing characteristics of single nanometric holes," Nano Lett. **5**(11), 2335–2339 (2005).
11. A. J. Haes, S. Zou, G. C. Schatz, and R. P. Van Duyne, "A Nanoscale Optical Biosensor: The Long Range Distance Dependence of the Localized Surface Plasmon Resonance of Noble Metal Nanoparticles," J. Phys. Chem. B **108**(1), 109–116 (2004).
12. J. N. Anker, W. P. Hall, O. Lyandres, N. C. Shah, J. Zhao, and R. P. Van Duyne, "Biosensing with plasmonic nanosensors," Nat. Mater. **7**(6), 442–453 (2008).
13. W. Fan, S. Zhang, B. Minhas, K. J. Malloy, and S. R. J. Brueck, "Enhanced infrared transmission through subwavelength coaxial metallic arrays," Phys. Rev. Lett. **94**(3), 033902 (2005).
14. A. Lesuffleur, H. Im, N. C. Lindquist, and S. Oh, "Periodic nanohole arrays with shape-enhanced plasmon resonance as real-time biosensors," Appl. Phys. Lett. **90**(24), 243110 (2007).
15. L. Pang, K. A. Tetz, and Y. Fainman, "Observation of the splitting of degenerate surface plasmon polariton modes in a two-dimensional metallic nanohole array," Appl. Phys. Lett. **90**(11), 111103 (2007).

#112672 - $15.00 USD Received 22 Jun 2009; revised 24 Jul 2009; accepted 25 Jul 2009; published 4 Aug 2009

16. J. Homola, *Surface Plasmon Resonance Based Sensors* (Springer-Verlag Berlin Heidelberg 2006), Chap.1.
17. F. Yu, and W. Knoll, "Immunosensor with self-referencing based on surface plasmon diffraction," Anal. Chem. **76**(7), 1971–1975 (2004).
18. H. B. Lu, J. Homola, C. T. Campbell, G. G. Nenninger, S. S. Yee, and B. D. Ratner, "Protein contact printing for a surface Plasmon resonance biosensor with on-chip referencing," Sens. Actuators B Chem. **74**(1–3), 91–99 (2001).
19. D. G. Myszka, "Improving biosensor analysis," J. Mol. Recognit. **12**(5), 279–284 (1999).

1. Introduction

Since the discovery of extraordinary transmission through subwavelength nanohole arrays [1], nanohole array have been used in surface plasmon resonance (SPR) sensors as an alternative to the prism-based Kretschmann–Raether configuration [2,3] and the diffraction grating approach [4]. While operating at normal or near-normal illumination, the nanohole array sensing configuration leads to a high packing density with a large number of parallel channels, which enables high resolution imaging with a wide field of view and a large space–bandwidth product [5,6]. Regular SPR and nanohole array sensing configurations possess well defined sensitivities that are determined by their excitation configurations and the corresponding propagating plasmonic mode dispersion relationships [7,8]. Alternative approaches utilize nanoparticle-based SPR, whose sensitivity depends on the near-field amplitude of the electric fields that are created by the excited localized surface plasmon resonances (LSPRs) used to detect the binding effects [9–12]. Although nanohole array based sensing configuration holds great advantage of potential high-throughput, the achieved limit of detection is still below the well-developed thin film based SPR sensor [8]. In order to improve the limit of detection by increasing the sensitivity of the nanohole array based sensor, the coupling between the LSPRs and propagating surface plasmon polaritons (SPPs) was investigated [13], and its potential to further increase sensitivity was proposed [14]. Additionally, suppression of the influences from environmental variations is also crucial. SPR sensor configurations detect a change in the refractive index, which is an overall manifestation of specific bindings, nonspecific binding events on the sensor surface, variations in the bulk concentration, and temperature fluctuations in the environment. Therefore, the improved sensing technique would also be susceptible to the background, making it impossible to accurately identify the biorecognition reaction in low concentrations.

In this manuscript, we present a composite mushroom-like metallodielectric nanostructure (MMN) as an alternative approach to couple these two types of plasmonic phenomena and exploit them for practical applications such as biorecognition reactions. The enhancement of the electric field amplitude due to the LSPR is combined with the propagating SPP in our composite nanoresonator design. With our approach, instead of nanoparticles, we use nanovoids to create nanoresonators to excite LSPRs. Moreover, these nanoresonant voids are arranged to create a periodic perforated structure that under the phase matching condition enable excitation of propagating SPP waves that are coupled to these nanoresonators. The composite nanoresonator structure was fabricated by combining holographic lithography with an oblique deposition process of metal, creating a 3-D MMN. The MMN was integrated with microfluidic channels to examine biorecognition reactions, showing more than one order of magnitude improvement in the limit of detection in comparison to that achieved with conventional sensor configuration exploiting SPP in metal film perforated with a 2-D nanohole array.

2. Method

The concept of a nanoresonant array structure is shown in Fig. 1(a), where nanoparticles are integrated into the 2-D metal film perforated by a nanohole array. The period is designed to satisfy the phase matching condition (i.e., momentum conservation) for excitation of SPP wave propagating along the metal surface. The excited SPP wave couples into the nanoparticles to excite LSPRs around the nanoparticles, enhancing the amplitude of the electric field on the surface of the nanoparticles, thereby increasing the sensing ability of the resonant structure. However, since the practical realization of such a structure on a large area

#112672 - $15.00 USD Received 22 Jun 2009; revised 24 Jul 2009; accepted 25 Jul 2009; published 4 Aug 2009

will be challenging (see Fig. 1(a)), we introduce a close alternative, its complementary arrangement, consisting of nanovoid to replace the nanoparticle for excitation of LSPRs (see Fig. 1(b)). This configuration can be easily realized. The proposed geometry is a layer of structured gold film on top of a perforated substrate, in which the film protrudes out over the perforated substrate, forming nanovoids. The size of the nanovoids can be controlled independently of the underlying cylindrical perforation. When SPP waves propagate, they are reflected by the gold barriers, interfering with each other and forming localized standing SPP waves. The LSPRs are also excited near apexes; since the propagating SPP resonance and the LSPR are coupled, these two mechanisms can be utilized to enhance the amplitude of the electric field.

The period of the MMN sensor chip is designed for operation at near normal incidence angle for excitation of SPP resonance, facilitating operation with large size arrays with parallel detections, while avoiding the interference of SPP modes at normal incidence [15]. To satisfy the phase matching conditions for excitation of propagating SPP (1, 0) mode on a water-metal (WM) interface, we use a period of 1.20 μm for operation at a wavelength of 1.55 μm at an incidence angle of 1.5 degrees. The excitation of the WM SPP mode is further validated using rigorous coupled wave analysis (RCWA) to calculate the far-field transmittance. Furthermore, we used finite element method (FEM) simulations, COMSOL, to investigate and compare the near field enhancement in the commonly used thin metal film perforated by 2-D array of nanoholes with that of the MMN substrate. We use an array periodicity of 1.20 μm, a nanohole size of 200 nm, a gold film thickness of 50 nm and refractive indexes of water and glass being 1.32 and 1.5, respectively.

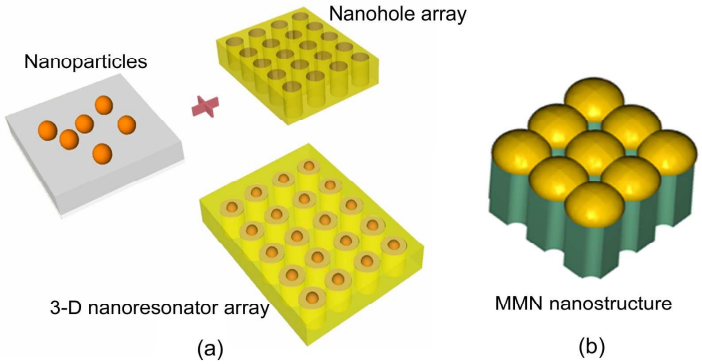

Fig. 1. (a) Conceptual diagram of a 3-D nanoresonator array structure combining LSPRs and SPP in a metal film perforated by 2-D nanohole. (b) Schematic diagram of the proposed nanovoid geometry for practical realization of LSPRs coupled with SPP in a 2-D metal film perforated with nanohole.

The MMN void size is 25 nm to excite the localized resonant LSPR as shown in Fig. 2(a) – 2(b). For comparison, Fig. 2(d) – 2(e) show the near-field distribution with the same scale for a conventional nanohole structure in a gold film with the same parameters as the resonant void in the MMN substrate. The incident electric field from the top is set at E_x = 1 (V/m) for both the MMN and the nanohole substrates in the FEM simulations. Figure 2(g) – 2(h) show the rescaled field distribution of the nanohole structure for clarification. As we know, the resonant conditions for the nanoparticle depend on its size and shape [12]. Our calculation reveals that the excitation of LSPR in the nanovoid also depends on the size of the void (or the gap) and the curvature of the apexes of the void edge. As shown in Fig. 2(a), 2(b), a LSPR is excited in the nanovoid with a 25-nm gap and a 25-nm apex radius of curvature, whereas no resonance is excited in the regular nanohole with a diameter of 200 nm as shown in Fig. 2(d) and 2(e). The rescaled Fig. 2(g) and 2(h) reveal the actual values of the electric field intensity. The combined incident and reflected beam intensity is even stronger than that inside the nanohole as shown in Fig. 2(g). Figure 2(h) shows that the field is concentrated at the nanohole corners, which has no resonant effects. The intensity of the electric field is about 1

#112672 - $15.00 USD Received 22 Jun 2009; revised 24 Jul 2009; accepted 25 Jul 2009; published 4 Aug 2009

$(V/m)^2$ in most of the nanohole area. Comparing Fig. 2(b) and Fig. 2(h), the enhancement factor for maximum intensity ($\left[\left|E_{x\_MMN}\right|^2\right]_{max} \Big/ \left[\left|E_{x\_nanohole}\right|^2\right]_{max}$) would be more than 100 times. On the other hand, in both cases, the propagating (1,0) WM SPP mode along the interface is also excited as indicated in Fig. 2(c), 2(f) or 2(i), in which the intensity of the electric field $\left|E_y\right|^2$ decays exponentially away from the metal surfaces (plot not shown). The enhancement factor for the maximum intensity $\left[\left|E_{y\_MMN}\right|^2\right]_{max} \Big/ \left[\left|E_{y\_nanohole}\right|^2\right]_{max}$ is about 7.5 times. In order to compare the electric field enhancement of our MMN substrate, amplitudes of the total electric field ($E_{norm} = \sqrt{|E_x|^2 + |E_y|^2}$) are calculated, which gives an enhancement for the maximum electric field ($\left[E_{norm\_MMN}\right]_{max} \Big/ \left[E_{norm\_nanohole}\right]_{max}$) of about 5.7. For sensing application, resonant shift relies on the average response of the attached molecules interacting with the electric field in certain region above the metal surface. Therefore, a 50-nm-subdomain integration of the electric fields above the gold surface and the gap space in between the gold rods were performed. It gives an enhancement factor of 2.6 ($\iint_{D\_MMN} E_{norm\_MMN} \Big/ \iint_{D\_nanohole} E_{norm\_nanohole}$), where D_MMN = 5.93×10^4 nm^2 and D_nanohole = 6.75×10^4 nm^2 refer to the integration area for the MMN and the nanohole structure, respectively, in a single periodic cell. Due to the difference in these two geometries, the integration area for the MMN substrate is slightly less than that of the nanohole. This near field electric field enhancement is due to the excitation and coupling between localized SPR and propagating SPP mode; therefore, the enhancement would affect SPR sensing activities as shown below.

This near field electric field enhancement is due to the excitation and coupling between localized SPR and propagating SPP mode; consequently, the enhancement may affect the SPR sensing activities through the sensitivity enhancement by the effective index shift and a decrease in the penetration depth of the electric field. The sensitivity for a sensor is defined as the derivative of the monitored resonant parameter (e.g., angle, wavelength, magnitude, or phase of the field) with respect to the parameter that needs to be detected (e.g., refractive index or concentration). The sensitivity depends on the method of the SPR excitation, interrogation configuration, and metal and dielectric properties. For biosensor, the sensitivity corresponds to surface refractive index change near the sensing surface, i.e., metal surface, also referred to as surface sensitivity. The verification of the sensitivity relies on the knowledge of the thickness and the effective index of the bio-layer above the sensing surface, which usually cannot be well defined in the experiment. Instead the limit of detection is used to characterize the sensor's capability. The limit of detection corresponds to the minimum change in the refractive index or concentration that can be detected with reasonable certainty.

In the semi-infinite metal and dielectric plasmonic sensor configuration, the surface sensitivity [16] can be expressed as

$$S_S = S_B \frac{2h}{L_{pd}} \sim \left(\frac{\partial n_{eff}}{\partial n}\right)_B \frac{2h}{L_{pd}} \qquad (1)$$

#112672 - $15.00 USD Received 22 Jun 2009; revised 24 Jul 2009; accepted 25 Jul 2009; published 4 Aug 2009

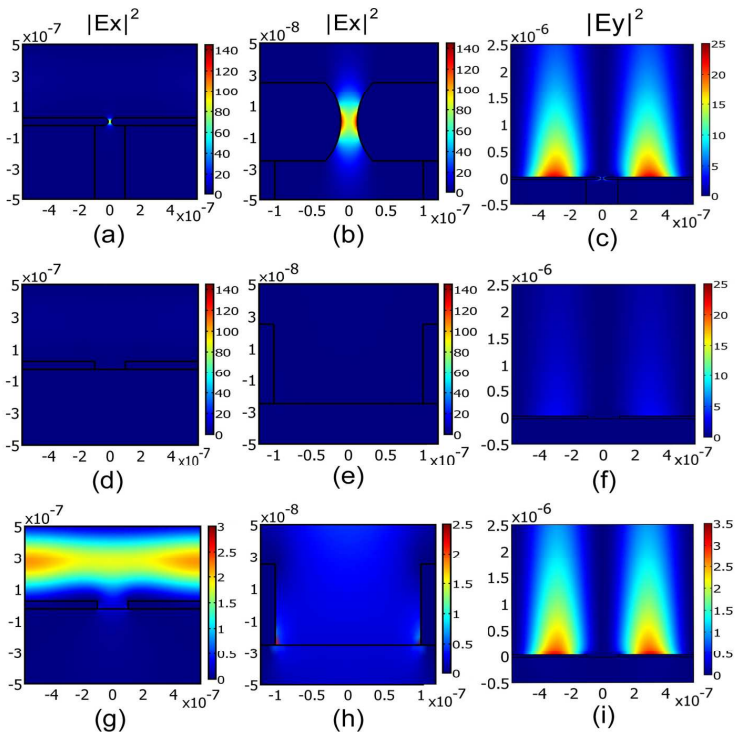

Fig. 2. Near-field FEM simulation for simultaneous excitations of LSPR and SPP. (a)-(c) The intensity distribution of the electric field in the MMN substrate on the water-metal interface. (d)-(f) The intensity distribution with the same scale for a conventional nanohole structure. (g)-(i) The rescaled field distribution of the nanohole structure. (a), (d) and (g) show the field intensity distribution in the x direction ($\left|E_x\right|^2$) or along the metal surface. (b), (e) and (h) are the close-ups of the nanoresonantor or nanohole area. (c), (f) and (i) correspond to the field intensity in the y direction ($\left|\mathrm{E_y}\right|^2$), or normal to the metal surface. The units for the dimensions are meters.

where S_S and S_B denote the surface and bulk sensitivity, respectively, h is the limited distance from the metallic surface whose index would change, n_{eff} is the effective index of the plasmon, and L_{pd} is the penetration depth, which is defined as the distance from the interface at which the amplitude of the field decreases by a factor of 1/e. For the sensing configurations presented here, the basic concept in Eq. (1) may still hold, which means that the surface sensitivity is proportional to the bulk sensitivity and inversely proportional to the penetration depth of the electric field. From Fig. 2(c) and 2(i), it can be clearly seen that the MMN substrate exhibits shorter penetration depth than that in the regular nanohole substrate. The reduction factor of the penetration depth is about 3.1/2.2 = 1.4. In addition, the effective index may also be affected due to the enhanced surface electric field originating from the excitation and coupling of the LSPR. We calculated the surface sensitivity enhancement through simulations by monitoring the peak resonant wavelength shift when we changed the refractive index of a thin layer from the surface of metal film. We used the same FEM simulations as shown in Fig. 2, but monitored the peak resonant wavelength in the far field S-parameter when a 50-nm-thick adlayer with a refractive index of 1.37 was added onto the gold surface to simulate a biosensing binding event. We conducted the simulations for both the MMN and the nanohole array substrates. The calculated surface sensitivities, defined by the ratio of resonant peak wavelength shift to the surface index change, are 30 and 6 nm/RIU, respectively, where

#112672 - $15.00 USD Received 22 Jun 2009; revised 24 Jul 2009; accepted 25 Jul 2009; published 4 Aug 2009

RIU denotes refractive index unit. The surface sensitivity is about 5 times higher for the MMN structure compared to the nanohole structure. It should be noted that the near field distributions shown in Fig. 2 and the enhancement factor calculation were conducted in a 2-D case, which would correspond to the metallic narrow 'slit' hanging above the 1D grating structures.

Fabrication of the MMN structure over a large substrate area is achieved by combining the holographic patterning technique with an oblique metal deposition procedure as shown in Fig. 3. First, holographic lithography is used to create perforation of a 1-μm-thick layer of UV resist. An anti-reflective coating (ARC) is used to prevent formation of fringe patterns resulting from multiple reflections in the substrate. The exposure is followed by the development procedures producing a structure shown in Fig. 3(b). The hole diameter can be adjusted by changing the exposure dosage due to the strongly nonlinear response of the UV resist. The next critical step consists of sputtering a controlled layer of gold from an oblique angle as the sample is rotated on the sputtering stage (see Fig. 3(c)). The thickness of the metal film is determined by the deposition rate, the deposition time, and the deposition angle (θ), whereas the void size is determined by two additional parameters: periodicity of the perforation and a filling factor. As the thickness increases, the void size decreases; thus, the size can be controlled precisely by controlling the sputtering time. Figure 3(d) shows a cross-section scanning electron beam microscopy (SEM) micrograph of a fabricated mushroom-like resonant structure. Although the cross section of the fabricated MMN substrate is affected by the cutting process of amorphous glass substrate and the rigid polymer layer, the demonstrated profile resembles the desired mushroom-like shape (see arrow). This can be further assessed by over deposition as shown in Fig. 3(e), where the array of voids has been sealed.

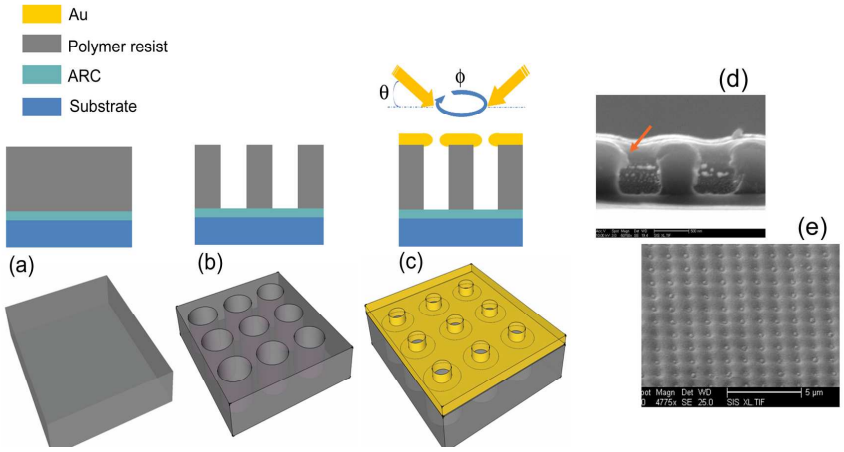

Fig. 3. Fabrication schematic of the nanovoid resonant. ARC is used to avoid back-reflection of UV light from forming fringes on the photoresist during the holographic lithography. (a) Processing of thick resist layer; (b) Exposure and development; (c) Oblique deposition of metal layer. The bottom drawing in each figure shows the 3-dimensional sketch in each procedure. (d) SEM photograph of fabricated composite metallodielectric nanostructure. (a) Cross section of the nanovoid structure. (e) Top view of the voids that had been sealed due to over deposition.

Next we integrate the MMN substrate with a microfluidic delivery chip to investigate a biorecognition reaction between immobilized receptor and analyte in a flowing solution by real time monitoring of the resonant transmission wavelength through the MMN device. The microfluidic delivery chip is fabricated in polydimethylsiloxane (PDMS) using soft lithography method. A chamber consisting of six $2000 \times 100 \times 50\ \mu m^3$ channels with 100-μm separation walls was then bonded to the composite MMN substrate by applying oxygen plasma bonding. In order to overcome the poor adhesion between PDMS and the MMN gold surface, the bonding was accomplished through an additional lithographic processing step

#112672 - $15.00 USD Received 22 Jun 2009; revised 24 Jul 2009; accepted 25 Jul 2009; published 4 Aug 2009

where patterned channel of thin SiO_2 film was deposited directly onto the MMN surface before attaching the PDMS channel. The upper right inset in Fig. 4(a) shows the assembled device, where the color illustrates the diffraction from the perforated array. Tubes connected to needles were inserted into the ports of the corresponding PDMS channels for on-chip optofluidic control and measurements. The assembled device was mounted on a precision rotation stage as shown in the upper left inset in Fig. 4(a), where three channels can be seen connected with tubes. The bottom of Fig. 4(a) shows the measurement setup layout and the microfluidic delivery system, which includes a microcontrolled pump (VICI Valco Instruments, M6 CP-DSM) with adjustable flow rate and a mechanism to control the flow rate using height adjustable syringes. The optical setup is illustrated in Fig. 4(b), where the assembled chip is mounted on a rotational stage (Physik Instrumente, M-037.PD) and illuminated by a polarized monochromatic laser beam (Newfocus Venturi Tunable laser TLB 6600), while directly transmitted background is filtered out by an orthogonally oriented analyzer [6]. The SPP resonant transmission signal is acquired by a power meter (Newport 818-IR).

3. Results

The dispersion relation of the WM SPP modes was measured by scanning both the wavelength and the angle of incidence (see Fig. 4(c)). We observe that for operation at semi-normal incidence of 2 to 4 degrees with an array period of 1.2 μm, the operating wavelength range will be 1520 - 1570 nm. The slight angle discrepancy from the simulation is due to the accuracy of the indices used in the simulation. The incident angle was set to be 3 degree to excite the WM (1, 0) mode with a resonant wavelength around 1536 nm.

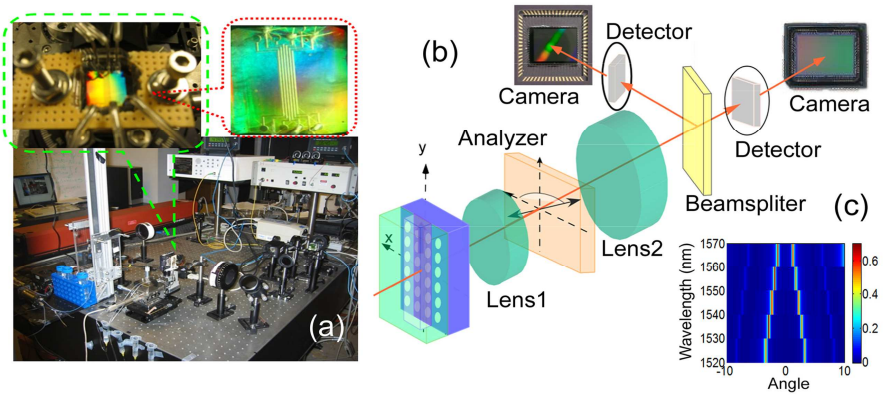

Fig. 4. (a) Measurement setup layout on the optical table and the microfluidic system. The upper left inset shows an assembled sensor chip with three channels connected with tubes and the upper right inset shows the microfluidic channels on the nanoresonant gold surface. (b) Schematic of the setup; (c) Angular spectra of the nanoresonant array sensor with water inside the channel; the two weak resonant spectra in larger angle of incidence correspond to PDMS-Au SPP modes.

This setup was used for real-time monitoring of the interaction between immobilized biotinylated bovine serum albumin and flowing streptavidin by observing the SPP resonant wavelength shift while keeping the incidence angle fixed. The experiment was designed to block the nonspecific binding and eliminate environmental variations (i.e., temperature, or pressure). Experiments were conducted in the signal and control channels. In the calibration experiment, the same reaction data were obtained in the signal and control channels when they were filled with the same solution from phosphate buffered saline (PBS) buffer solution to biotinylated bovine serum albumin (BSA) immobilization to streptavidin interaction. A series of experiments on recognition reactions with different streptavidin concentrations were also conducted (not shown).

#112672 - $15.00 USD Received 22 Jun 2009; revised 24 Jul 2009; accepted 25 Jul 2009; published 4 Aug 2009

After a sensor chip was assembled, the signal channel was filled with biotinylated BSA of 50 μg/ml in PBS with 1% 2-mercaptoethanol for more than 2 hours. The control channel was filled with BSA of the same concentration for the same time duration. Then both channels were connected to a single input afterward to experience the same flow rate. First, 50 μg/ml of BSA solution was introduced into both channels for twenty minutes to cover any possible bare Au surface, blocking any possible streptavidin nonspecific binding sites. Both channels were then washed with PBS and then real-time monitoring commenced as shown in Fig. 5(a). The red and blue curves correspond to the control and the signal channels, respectively, which exhibit 0.6 nm resonant bias. The sensor chip was mounted on a custom ordered thermo-electric cooler (TEC) module. The center portion of the TEC was removed and the substrate of the sensor chip was mounted onto the edge of the TEC module. First, the temperature was set at a room temperature of 23.5° C. After about 40 min, the temperature was raised to 55° C, and then reduced back to 23.5° C. The change in the environmental temperature is clearly evident in the real-time detection as shown in Fig. 5(a). When the temperature increased, the resonant response dropped rapidly due to the decrease in the refractive index of PBS. After the temperature was reset back to 23.5° C, the resonant response restored slowly.

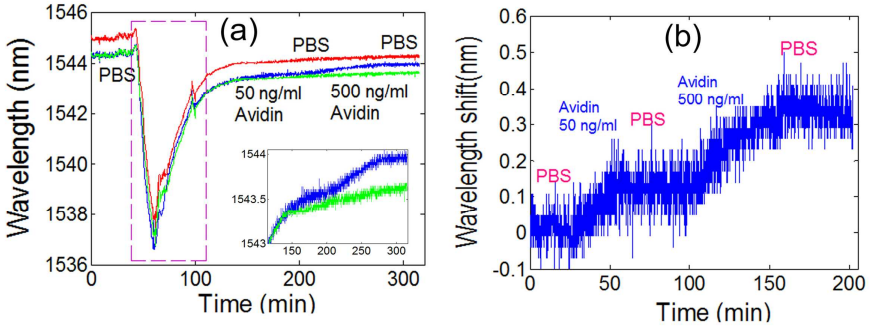

Fig. 5. (a) Real-time monitoring of binding between biotinylated BSA and streptavidin following the immobilization of biotinylated BSA in the signal channel and BSA in the control channel. Red, green, and blue curves correspond to control, shifted control, and signal channels, respectively. The inset in (a) is a close-up in signal and shifted control channels after they reached the same temperature. (b) Relative wavelength shift for the binding reactions by subtracting the shifted control (green) from the signal channel (blue).

After about 140 min, the resonant response had shown very slow change. Then 50 ng/ml of streptavidin was introduced into both channels. The resonant shift in the signal channel (blue curve) started increasing relatively quickly, while the control channel (red curve) exhibited constantly slow change. After about 60 min, PBS was introduced into both channels for about 30 min, followed by 500 ng/ml of streptavidin for additional binding test. The resonant response in the signal channel started to shift more rapidly until it reached saturation, whereas the control channel maintained the same pace. Finally PBS was introduced into both channels, washing away the unbound streptavidin in both channels. In order to clearly see the biochemical reactions in the control and signal channels, the bias between the two channels was removed by shifting the control channel response by –0.6 nm, which resulted in the green curve in Fig. 5(a). Compared with the shifted control curve, the specific binding in the signal channel can now be seen more clearly. Comparing the shifted control (i.e., green curve) and the signal (i.e., blue curve) channel, the two curves almost overlap before the introduction of streptavidin, except for the rapid temperature change as indicated by the dotted box in Fig. 5(a). The difference in the resonant response in the box indicated the non-uniform temperature distribution in the two channels, which resulted from the relative position difference of the two channels on the TEC module and could be resolved by prolonging the heating or cooling cycle for uniform heat distribution. The ripples on the two curves appeared as a result of the rapid pressure shift in the pump system. The consistency of these ripples in the two curves confirmed them to be a systematic error. When the temperature of the sensor chip slowly

#112672 - $15.00 USD Received 22 Jun 2009; revised 24 Jul 2009; accepted 25 Jul 2009; published 4 Aug 2009

decreases, reaching room temperature, the two curves (blue and green) overlapped again. As seen in the inset, which is a zoom-in of the blue and the green curves in Fig. 5(a) after reaching room temperature, the slow evolution of the control curve indicates nonspecific binding and temperature drift in both channels. These environmental influences can be eliminated by subtracting the control response from the signal channel as shown in Fig. 5(b), whose origin was reset. Figure 5(b) clearly shows the different reaction stages from PBS base line, 50 ng/ml streptavidin binding, PBS washing, 500 ng/ml streptavidin binding, and final PBS washing. The 50 ng/ml streptavidin binding gives 0.13 nm resonant shift. Considering the standard deviation of 15 pm for the current setup, obtained from monitoring the resonant drift of PBS, with 3 times the standard deviation, the limit of detection would be 17 ng/ml (0.3 nM), which is much lower than 3 μg/ml (26 nM) achieved with regular nanohole array sensor [8]. The improvement in the limit of the detection arises from the surface sensitivity enhancement due to the excitation of LSPRs and the improvement in the signal acquisition by the use of a control channel for eliminating nonspecific binding reactions.

From Fig. 5(b), we can see that the data is noisy, which will affect the accuracy of the limit of detection calculation. In general, the sensor noise originates from the optical source and electronic readout. Dominant sources of noise are fluctuations in the light intensity, scanning wavelength repeatability of the laser source, and photocurrent noise in converting light intensity into photoelectrons by the detector and the supporting circuitry. In the measurement, we scanned the wavelength of the laser, defined the resonant peak wavelength through a basic centroid method, and plotted the wavelength versus time. Averaging among multiple wavelength scans was not employed before tracking the peak wavelength. By averaging multiple wavelength scans, we can reduce the noise resulting from the laser intensity fluctuation and the wavelength variation. We used a power meter head as a detector, whose shot noise is higher compared to either a cooled low-noise PIN or APD detector, which we plan to use in the future. We believe that the above measures would lower the standard deviation of the system and improve the limit of detection of our sensing system even further.

4. Discussions and conclusions

As evident from Fig. 5(a), both the resonant response in the control and the signal channel are shifted by about 1 nm after they "recovered" from the temperature change. This could have resulted from a mechanical error of the rotation stage. This issue will be resolved in our future prototype system. Another possible reason for the partial shift could be due to the disassociation of immobilized biotinynated BSA and BSA. Nevertheless, these shifts did not affect the final experimental result because these factors occurred in both channels and were eliminated to obtain only the specific binding events by subtracting the control response from the signal channel. As we pointed out, the near field distributions shown in Fig. 2 were carried in 2-D, which may not reflect the actual configuration. For 3D simulation, although the principle of the enhancement would be the same, the actual local resonant shape and size will shift in terms of excitation wavelength and the angle due to the shift in the effective refractive index. The format of the local resonant field would change and the sensitivity enhancement factor for the 3D structure would be affected by this factor. Further evaluation of the near field enhancement by using 3D simulation model and detailed analysis are being conducted and will be presented later.

A composite nanoresonant structure with nanovoids in metallic film was presented and demonstrated to have enhanced sensitivity in biorecognition reactions. The enhancement is realized by coupling the LSPR from the propagating SPP, resulting from the periodic perforation under the phase matching condition. The fabrication method introduced here represents a cost-effective way to build the composite nanostructures in which the chips are reusable and reconfigurable, since the metallic layer can be stripped away and re-deposited with a different nanovoid diameter. Although the control channel concept was introduced for prism-based sensing configurations [17–19], here the control channel was employed to improve the limit of detection of nanoresonant SPR sensor by taking advantage of its potential for large amount of parallel detection characteristics. Nonspecific binding and environment

#112672 - $15.00 USD Received 22 Jun 2009; revised 24 Jul 2009; accepted 25 Jul 2009; published 4 Aug 2009

vibrations were eliminated by the extraction of the control channel from the signal channel. Moreover, specific binding was verified to be still efficient after certain heating process. By using the nanoresonant, the limit of detection is improved to sub-nM, a substantial improvement to the tens of nM in conventional nanohole array SPR sensor. A prototype setup with various concentration arrangements is being built for comprehensive evaluation based on hundreds of detection spots using a CCD camera or detector array.

Acknowledgement

This work was funded by the DARPA Center for Opto-Fluidic Integration, NSF NIRT Program and NSF's CIAN ERC.

#112672 - $15.00 USD Received 22 Jun 2009; revised 24 Jul 2009; accepted 25 Jul 2009; published 4 Aug 2009